Chapter 13
Inkjet Printing and Other Direct Writing Methods

Paul G. Clem and Nelson S. Bell

13.1 Introduction

In recent years, a large effort has been focused on the deposition of metallic systems via advanced printing techniques, e.g. direct write, inkjet and μ-contact printing. Such printing techniques are attractive alternatives to conventional photolithography and electroless routes, which are time-consuming, complicated, and expensive. With the emergence of flexible electronics, the ability to integrate dissimilar materials, i.e., ceramics, metals, semiconductors, and polymers, onto a single, temperature-sensitive substrate enables the fabrication of volumetrically-concise, multi-functional packages. In the past, the technical advances in low temperature co-fired ceramic (LTCC) packages allowed for integration of screen-printed metal traces at temperatures of approximately 800–900 °C. Coupling "drop-on-demand" deposition technologies with ink formulations based on nanoparticle, chemical solution precursors, and/or UV-curable chemistries provide lower-temperature, <200 °C, routes for deposition of highly conductive traces on polymeric commercial substrates. This presents an alternative maskless, cost-effective route to that of electrodeposited cladded substrates.

13.2 Development of Printable, Low Process Temperature Metal Inks

A major challenge in applying advanced printing techniques for the deposition of functional materials is the formulation of suitable inks. Ink chemistry and formulation determine not only the as-deposited characteristics, but also ink stability. The ability to deposit well-defined, uniform, and high quality print patterns without

P.G. Clem (✉) • N.S. Bell
Sandia National Laboratories, Albuquerque, NM, USA
e-mail: pgclem@sandia.gov

T. Schneller et al. (eds.), *Chemical Solution Deposition of Functional Oxide Thin Films*,
DOI 10.1007/978-3-211-99311-8_13,

clogging the print head requires a fundamental understanding of the ink chemistry and the corresponding processing-property relationships. While the ability to deposit a suite of metallic compositions (Ag, Cu, Au, Al, Pt, Pd, etc. . .) is desirable, the following section details several routes for the deposition of low-temperature curing silver-based ink designs.

13.2.1 Nanoparticle Synthesis

Conventional low-temperature co-fired ceramic (LTCC) technology involves the production of multilayer circuits from ceramic substrates. Conductive and insulating thick films are screen-printed onto each LTCC as needed, facilitating monolithic structures of embedded resistors, capacitors, and interconnects. Often, thick film conductor formulations consist of (1) silver flake, a highly anisotropic, micron-sized particulate, (2) organic binder, and (3) a glass frit to reduce sintering temperatures (bulk Ag $T_m = 963$ °C). Sintering of LTCC at "low" temperatures, e.g. 850–900 °C, allows for the integration of low resistivity conductors, i.e., Ag, with LTCC packages.

It is now well-established that by shrinking the size of a solid particle to the nanometer scale, one can alter its chemical, thermal, electrical, mechanical, and optical properties. With respect to melting temperatures, the presence of high curvature nanoparticles has been proposed to either generate a low-temperature sintering reaction, or else a high curvature-driven driving force for low temperature necking and conductivity development. Nanoparticle reactivity has been characterized experimentally to be much higher than classical thermodynamic predictions. Dominguez et al. [1] proposed the size dependence of surface melting on the basis of a Debye model with the Lindemann law and incorporated a phonon softening process according to the following equation:

$$T_m = \frac{Mk\Theta_b^2\delta^2a^2}{36\hbar^2\left[1-(1-\mathrm{na/R})^3\right]} + \frac{1}{8}\Theta_b \tag{13.1}$$

where M is the atomic mass, k is Boltzmann's constant, $\hbar$ is Plank's constant, δ is the Lindemann law parameter for liquifaction ($\delta = 0.5$), a is the lattice parameter, Θ_b is the bulk Debye temperature, r is the nanoparticle radius, and na is the surface thickness where melting occurs, ($n = 3.5$). Equation (13.1) provides a good estimate of the temperature where sintering initiates and the relationship for silver is illustrated in Fig. 13.1. This predicts sintering to occur at room temperature for particles smaller than 25 nm due to increased nanoparticle reactivity.

Of the many various existing preparation schemes for Ag nanoparticle synthesis, the simplest and most commonly used synthesis route is the chemical reduction of a silver salt by a reducing agent, e.g., sodium borohydride, citrate, or ascorbate. The reduction of metallic ions leading to neutral atoms, the building blocks of metal

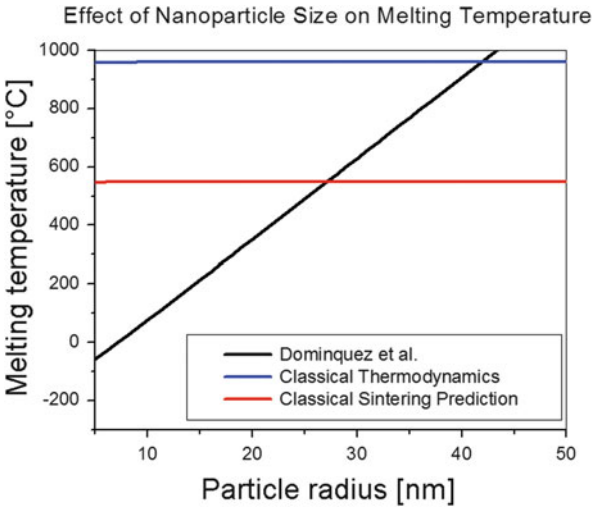

Fig. 13.1 Theoretical predictions of size-sintering relationship for silver nanoparticles

particles, is the result of a redox reaction in which electrons from a reducing agent are transferred to the metal according to:

$$m\mathrm{Me}^{n+} + \mathrm{Red} \rightarrow m\mathrm{Me}^{0} + \mathrm{Ox} \tag{13.2}$$

The driving force of the reaction is the difference between redox potentials of the two half cell reactions, ΔE. The magnitude of ΔE determines the value of the equilibrium constant of the reaction, K_e, according to the Nernst equation:

$$\ln K_e = n\mathrm{F}\Delta\mathrm{E}/\mathrm{RT} \tag{13.3}$$

where n is the number of electrons transferred, F is the Faraday constant, R is the universal gas constant, and T is the absolute temperature. The reduction reaction is thermodynamically possible only if ΔE is positive, which implies that the redox potential of the reducing agent must have a more negative value than that of the metallic species. Thus, strongly electropositive metals, like Ag, will react even with mild reducing agents under ordinary conditions. Through reducing agent selection and tuning of experimental parameters (i.e., solvent selection, temperature, and time) the resulting particle size, distribution and morphology can be tailored.

To prevent particle agglomeration, many studies have assessed the role of stabilizers and complexing agents (e.g. reverse micelles, surfactants, dendrimers, alkanethiols, and carboxylic acids) on suspension stability, particle size/distribution, and morphology. The ability to prepare high volume fraction, monodisperse, and spherical nanoparticle (<100 nm) inks would both minimize clogging during deposition and enable high density, as-deposited metal traces. A common complication in low-temperature reaction to a pure, highly conductive metallic state is slow thermal decomposition of organic stabilizers, as illustrated in Fig. 13.2. Often, silver nanoparticle suspensions use high molecular weight polymers as dispersants,

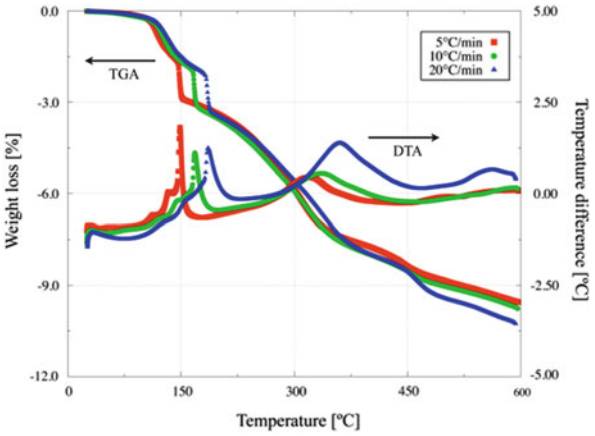

Fig. 13.2 Thermal analysis of silver nanoparticles (<10 nm) stabilized with a long chain carboxylic acid

requiring slow ramp rates and high temperatures to ensure complete conversion. Figure 13.3 shows the time\temperature dependence of DC resistivity of a silver nanoparticle ink stabilized with a long chain carboxylic acid at two different annealing temperatures, 100 °C and 170 °C, on either side of the dispersant decomposition temperature. The corresponding *in-situ* high resolution TEM analysis illustrates the necking processes that initiate around 100 °C. Perelaer et al. demonstrated high conductivity values (56 % of bulk silver) at 80 °C by using very small amounts of organic additives, using weakly adsorbing species such as amines, amides, and mercapto groups [2].

Wakuda and co-workers reported a room temperature sintering route for Ag nanoparticles using a chemical dip treatment utilizing an alkylamine dispersant—dodecylamine [3]. During particle synthesis, the nanoparticles are coated and stabilized with dodecylamine, and the resulting sterically-stabilized suspensions are patterned on glass substrates or copper plates. For dispersant removal, the sample patterns are washed in methanol, resulting in pure metallic particles which sinter upon removal of the solvent at room temperature [3]. Upon completion of a 2 h methanol submersion, microstructural observations revealed that the Ag nanoparticles had agglomerated and coarsened, with a measured DC resistivity of 7.3×10^{-5} Ω•cm; this is often normalized to the bulk conductivity of silver, 1.6×10^{-6} W-cm, or 45× bulk Ag ρ, in this case. Metal nitrate precursors, nanoparticle silver inks, and laser sintering enable low-temperature or even room temperature cure inks. Table 13.1 provides a summary of achieved conductivity values via different thermal treatment methods.

The use of strong reducing agents, i.e., borohydride, results in small particles that are somewhat monodisperse, but controlling particle growth is difficult. Additionally, such reducing agents may be associated with environmental toxicity or biological hazards. It has been, therefore, of increasing interest to develop "green" synthesis of colloidal silver nanoparticles. Research on chemical production routes utilizing green principles has increased in the past decade, where the most commonly used protecting agent is starch. The initial reference to "green" chemical

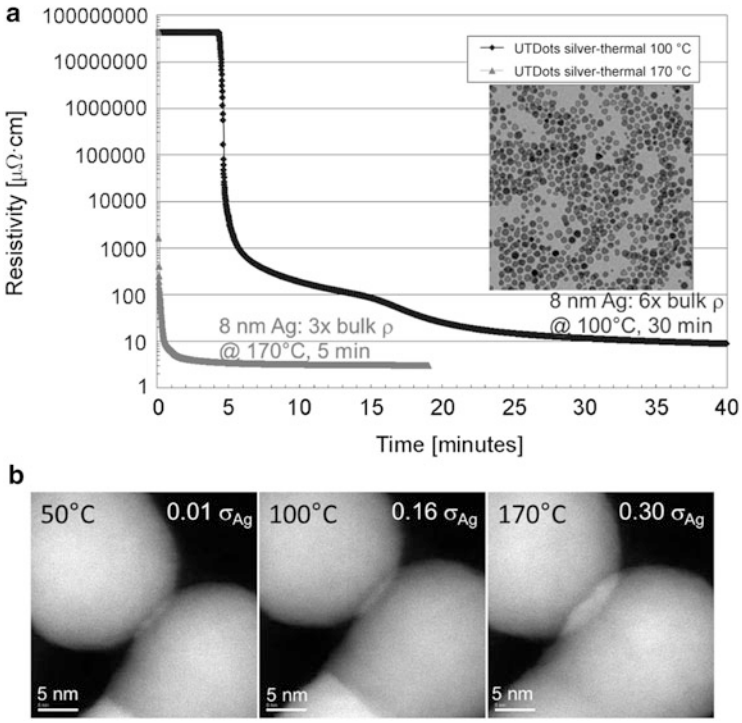

Fig. 13.3 (**a**) Time dependence of DC resistivity for direct written Ag traces. (**b**) HR-TEM demonstrating the necking and growth mechanisms of silver nanoparticles. HR-TEM images courtesy Prof. D. Kovar and P. Ferreira at University of Texas-Austin

Table 13.1 Summary of print method properties, and metal resistivities vs. thermal treatment

Topic	Method	Details
Printable area		
Area: 1 m^2 area, 60 cm Δz	Syringe or aerosol jet	
Resolution: ≥16 μm	Syringe or aerosol jet	Working toward 5 μm
Conductors (traces and via-fills)		
Silver precursor (nitrate)	5× bulk Ag ρ	400 °C
25 nm silver nanoparticle inks	3× bulk Ag ρ	300 °C
5 nm silver nanoparticle inks	3× bulk Ag ρ	170 °C
Laser sintering	4× bulk Ag ρ	25 °C

routes to Ag nanoparticles was by Raveendran et al., who used β-D-glucose as a reductant and starch as a protecting agent [4]. Silver nanoparticles were formed at 40 °C over the course of 20 h. Alternatively, maltodextrins are polysaccharides derived from starch by either acid or enzymatic preparation routes, leading to partial hydrolyzation. As starch and glucose are applied to silver nanoparticle synthesis, the product is expected to serve as a copolymer that would provide

both the reduction and stabilization properties for nanoparticle silver synthesis. Bell and Lu [5] have recently utilized the maltodextrin route for room temperature synthesis of silver nanoparticles. The reactant molecule is a partially converted carbohydrate containing reducing sugar groups and having low molecular weight. To date, most "green" chemistries of silver derived nanoparticles focus on commercial anti-bacterial activity application such as catheters, dental materials, and textile fabrics, but efforts are carrying over into conductor applications.

13.2.2 Metallo-organic Precursor Routes to Silver Inks

For over a century, metallo-organic solutions have been used for the deposition of metal films, e.g., decoration on ceramics and silvered-glass mirrors. Only recently, however, have metallo-organic decomposition (MOD) designed inks been seriously investigated for use in electronics applications. As an alternative route to a particle based formulation, this is a true solution route. The silver molecular complex is very stable, even at concentrations up to saturation; neither requiring additional stabilizers nor reducing agents. The critical factor in development of MOD conductive inks is the selection of precursor chemical compounds. The precursor chemical structures should be designed to convert to conductive metals at relatively low temperatures and at high purity levels. Finally, the selected chemical precursors must be soluble in general organic solvents, produce uniform films, have a long shelf life, and adhere well to a wide range of substrates. Due to ease of preparation and high yield, silver carboxylate precursors are commonly used. Figure 13.4 illustrates thermal decomposition characteristics of several silver carboxylates.

One of the origin examples of ink design for an advanced printing application was reported by Teng and Vest [6]. To pattern collector grids on silicon wafers for photovoltaic solar cells applications, ink solution formulations were prepared with silver neodecanoate dissolved in xylenes (which is stable up to 20 wt% Ag). Through inkjet printing and thermal treatment at 300 °C of the MOD derived inks, the authors were able to avoid degradation of the p-n junctions, produce uniform line traces on the surface of the solar cells, and increase the overall efficiency of the solar cells. Dearden et al. used a similar experimental approach to evaluate conductivities of printed Ag neodecanoate lines from 125 to 200 °C [7]. Resistivity values were reported to approach 2–3 times the bulk resistivity values for thermal treatment conditions greater than 150 °C. Recently, it has been reported that β-ketocarboxylate derived silver inks can be cured as low as 95 °C on paper based substrates. It is interesting to note that one of the lowest reported decomposition temperatures is that of silver oxalate, ~100 °C. Unfortunately, the salt decomposes so exothermically that maintaining dense printed features proves to be difficult.

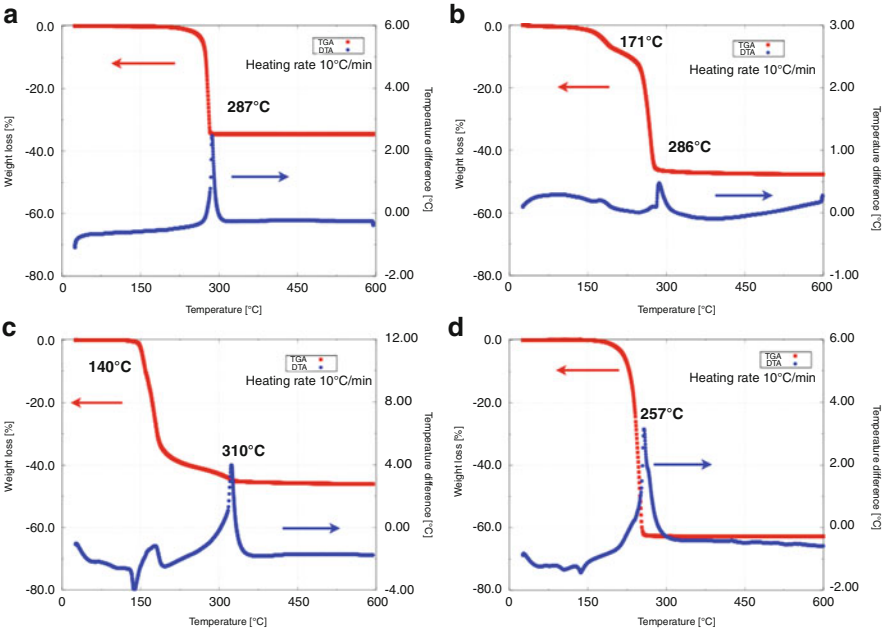

Fig. 13.4 TGA-DTA analysis of the decomposition characteristics for (**a**) silver acetate, (**b**) silver 2-methoxy[2-ethoxy(2-ethoxy)] acetate, (**c**) silver lactate and (**d**) silver neodecanoate

13.3 Inkjet, Microcontact and Nanocontact Printing of Solution Precursors for Oxides and Metals

Inkjet printing of functional oxide materials is relatively recent in development, and places difficult demands on ink formulation, surface tension, vapor pressure and chemistry [8]. These issues have recently been overcome by leading groups, utilizing novel ink chemistries and processing. Inkjet printing generally utilizes low viscosity inks, of viscosity 1–10 mPa-s, or 1–10 cP (centipoise). These may be dispensed by piezoelectric, pneumatic, or thermal (bubble jet) methods, in which ink is forced from a chamber, forms a droplet due to Rayleigh instability, and is ejected toward a substrate. Due to the low viscosity required, as well as need to avoid ink drying and clogging of the print head, low volume fraction inks with surface tension and humectant (low vapor pressure) additives are often used. A wide variety of materials have been printed using these methods, initially for graphic, and more recently for high performance electronics printing and even superconductor printing. Van Driessche and Glowacki have demonstrated printing of both high quality buffer layers and superconducting YBCO layers using ink jet printing of chloride and trifluoroacetate precursors [9, 10]. The ability to print precursors which may subsequently be converted to epitaxial or biaxially oriented films is a significant advance for inkjet printed electronics, and is potentially

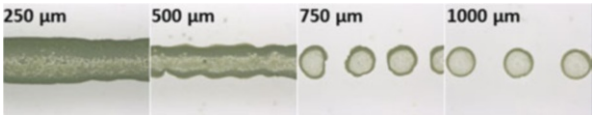

Fig. 13.5 Inkjet printed Al-doped ZnO (AZO) as a function of drop-to-drop spacing, illustrating transition from continuous lines to disconnected droplets

scalable to long lengths by utilizing commercial high rate inkjet printing systems originally designed for graphics printing. Printed electronics for display applications, utilizing complex oxides such as aluminum oxide, indium tin oxide (ITO), aluminum doped zinc oxide (AZO), indium gallium zinc oxide (IGZO), and alloys of these have also been printed from chloride and carboxylate precursors, which enables high mobility transparent conducting oxides for printed inorganic thin film transistors (TFTs), photovoltaic, and other printed electronics applications [11–13]. Use of chloride precursors in water or alternative solvents may simplify complications of using traditional metal alkoxide or metal carboxylate precursors, which often utilize highly volatile solvents, and may display condensation reactions in ambient humidity, which can complicate inkjet printing. Inkjet printing typically deposits small droplets, which can be overlapped to form continuous traces and uniform lines. Precursor drying, surface tension, and ink stability must be engineered carefully to enable uniform printed electronics with predictable material properties (Fig. 13.5).

Alternative methods to inkjet printing, with the potential for high throughput manufacturing, and possibly higher volume fraction inks, include roll to roll printing methods such as gravure and contact printing. Gravure printing of solution precursors is particularly attractive for printing transparent conductive oxides as transparent thin film transistors (TFT) for liquid crystal displays, and for solar cell manufacturing. In these printed electronics methods, the viscosity and surface tension are critical for high precision and reliability printing, while solution chemistry and materials science likely controls printed materials performance. As three examples of printed electronics, our group used copper, yttrium, and barium acetate precursors to print $YBa_2Cu_3O_{7-\delta}$ superconducting films (cp. Chap. 27), crystallized in an oxygen-containing atmosphere, Cu metal conductive traces, reduced from CuO using a reducing atmosphere of 4 % H_2/96 % N_2, and Al:ZnO transparent conductive oxides [14].

In this method of solution stamping nano-lithography an elastomeric stamp containing relief patterns is first coated with a sol-gel precursor solution of inorganic (functional oxide or ceramic) materials, and then placed on a surface to transfer the precursor from the stamp to the substrate, as shown in Fig. 13.6. Polydimethysiloxane (PDMS) is widely used as the stamping material, although vinyl or other polymers may also be used, if alternate physical or chemical properties are desired. Due to the flexible mechanical properties of the PDMS elastomeric material, the stamp forms a conformal contact with the surface. Ink transfer only occurs at locations where the stamp contacts the surface because of the

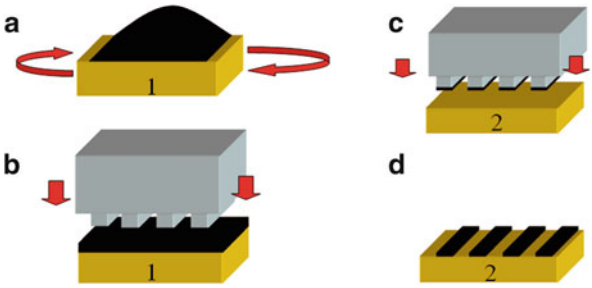

Fig. 13.6 Schematic of transfer printing of a solution precursor from a substrate or platen (1) to a patterned stamp and onto a substrate (2)

stamp morphology. Hence, the resulting patterns on the substrate mirror the stamp relief structures. For effective transfer from an initial coated substrate or platen, an effective method is for a coated precursor to evaporate some solvent, but remain a liquid with a high viscosity; an effective means of accomplishing this is to use a low volatility solvent such as an ethanolamine, glycol or glycerine additive to a traditional alkoxide solution precursor. The stamped patterns of this viscous, low vapor pressure organic precursor are then processed following standard thermal procedures, such as heating to 300–600 °C, to convert them to the final composition of the desired inorganic material. Resolution may be decreased to very fine, submicron feature sizes. Figure 13.7 (top) shows stamped precursors of copper acetate and ethanolamines, demonstrating features as fine as 200 nm. Figure 13.7 (bottom) displays images of three micron lines of the transparent printed copper precursor, and the resulting metallic copper traces produced following oxidation of the precursor to CuO at 500 °C, followed by a reducing atmosphere anneal at 250 °C to form Cu metal. The printed traces displayed resistivity of 2.1 mΩ-cm, around 80 % of the bulk conductivity of copper [14].

For applications in which crystalline alignment is required, such as superconducting and electrooptic applications, the ability to deposit epitaxial films is of interest. Using conventional methods for processing oxide thin films via non-hydrolyzed precursors on a lattice-matched substrate, the patterned thin films may be epitaxially registered to the substrate. Epitaxial deposition of 100 nm thick superconducting YBCO films on $LaAlO_3$ has been demonstrated with this method, using a variant of the trifluoroacetic acid precursor system, to which low volatility diethanolamine and triethanolamine were added. This precursor was solution transfer printed as 50 micron wide stripes onto $LaAlO_3$, pyrolyzed by rapid thermal annealing at 325 °C, and crystallized at 780 °C. The resulting YBCO film displayed epitaxial registry with the $LaAlO_3$ substrate, as shown in Fig. 13.8, an onset critical temperature T_c of 85 K, and a critical current density of 600 kA/cm^2, measured assuming perfect continuity within the 50 μm printed lines across the 1 cm substrate [15]. The ability to print patterned YBCO lines is of interest for reducing alternating current (AC) losses for AC superconducting magnet and motor applications, and may be a much less costly process than subsequent photolithography.

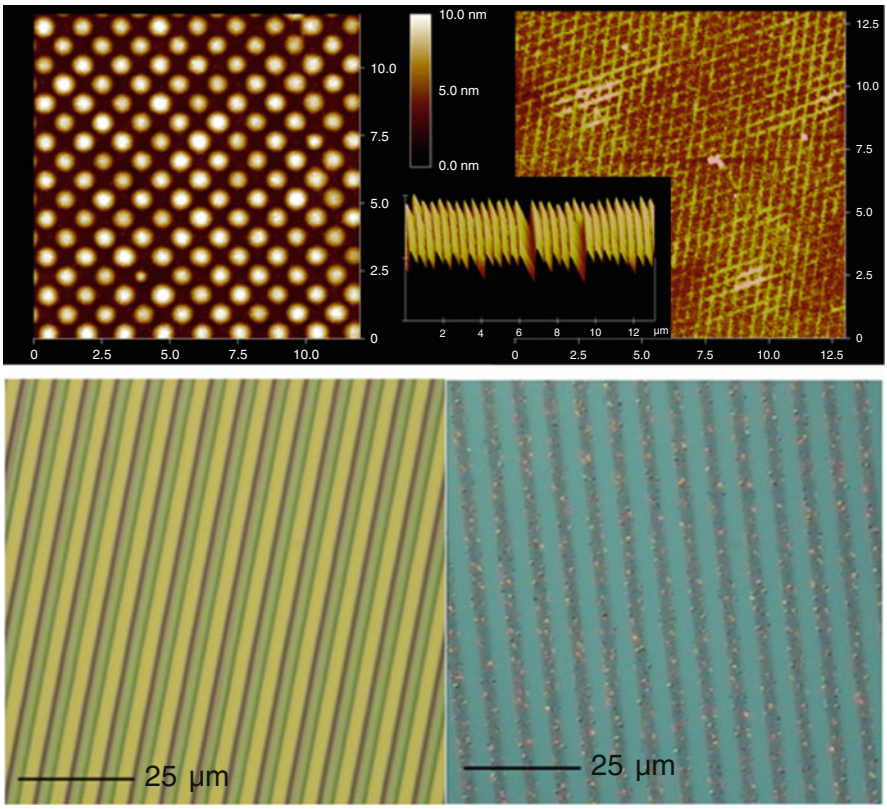

Fig. 13.7 *Top left*, 650 nm printed copper nanodots imaged by a 12 × 12 μm AFM scan. *Top right*, 12.5 × 12.5 micron AFM scan image of 200 nm lines of Cu printed using a PDMS stamp cured atop a standard diffraction grating. The inset shows the topology of the dry PDMS stamp. *Bottom left*, printed copper acetate/diethanolamine precursors on silicon, and *bottom right*, the printed copper pattern after oxidation to 500 °C in air, and post-anneal at 250 °C in 4 % H_2/N_2

13.4 Application Examples: Printed Strain Gages and Load-Frame Testing

Printable electronics may find application in green energy for increasing the reliability and performance of photovoltaics and wind turbine systems. Development of these technologies is of interest since rising energy prices and carbon emission standards are driving development of alternative energy sources including biofuel, solar, wind, and clean coal. A decrease of 20–50 % in wind energy cost for renewable resources is an aggressive goal, motivating interest in new technologies to decrease system manufacturing cost, optimize power generation efficiency, improve reliability, and decrease operation and maintenance costs [15–17]. A promising technology to improve wind turbine efficiency is smart rotor blades

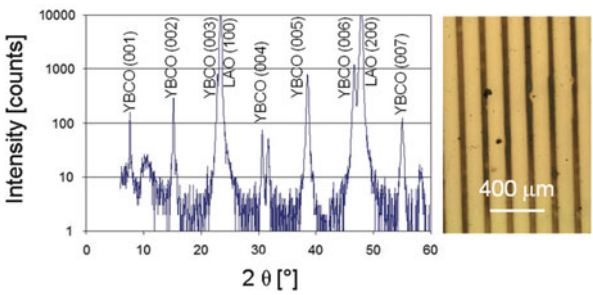

Fig. 13.8 X-ray diffraction and optical image of printed 50 µm width, 100 nm thick YBCO stripes on $LaAlO_3$ single crystal substrates, demonstrating epitaxial growth and continuous superconducting filaments

that monitor the physical loads being produced by the wind and adapt the airfoil for optimized energy capture. For extreme wind speeds and gust events, the airfoil could be changed to reduce the loads to prevent excessive fatigue or catastrophic failure. Prior Sandia work has developed an understanding of sensor placement sensitivity and methods for integrating internal strain and temperature sensors via fiber optic Bragg gratings [15]. However, sensor optimization in more complex blade models would require larger numbers of sensors [16], which is complicated by poor adhesion of surface mounted sensors, wiring of long (9–45 m) blades, altered aerodynamics, and high anemometer cost [17]. These opportunities for instrumenting generation systems to improve monitoring and reliability require placement of robust sensor networks into complex environments to provide diagnostic state of health information. Utilizing nanoparticle silver inks and an Optomec Aerosol Jet M^3D print system, high resolution strain gages were produced by printing silver inks directly on commercial wind turbine blade test sections provided by Sandia's Wind and Water Power Technologies department. The wind turbine blade composites consist of 50 volume % E-glass fiberglass in an epoxy resin such as Hexion Infusion resin MGS® RIM 135 and hardeners MGS® RIMH 134—RIMH 137. The fiberglass-epoxy composite is coated with a UV-stable urethane epoxy coating, providing a flat, impermeable external surface, on which the silver nanoparticle inks and copper 55 %/nickel 45 % solution precursors were printed and annealed. Images of printed silver and constantan inks on Kapton and wind turbine sections are shown in Fig. 13.9.

Commercial foil-based strain gages utilize a Wheatstone bridge configuration to measure both transverse and longitudinal strain, and typically use values of 120 Ω, 400 Ω or 1,000 Ω. Designs compatible with 120 and 1,000 Ω bridge operation were developed and printed as shown in Table 13.2. The 1,000 Ω samples were accurate to within 0.24 % of design resistance:

Blade sections with these highly accurate printed resistance bridges were loaded to 5,000 lbs., which was the limit of the wedge-loaded grips in the load frame tester. The resulting strains were in the area of 4,000 microstrain, as measured by a 1″ calibrated MTS extensometer. Using the 1,000 Ω resistors, which matched the internal resistors of the strain gage measurement electronics, the strain on the turbine blade section was cycled from −50 microstrain to +4,300 microstrain to measure the longitudinal and transverse strain response of the printed gages. In each

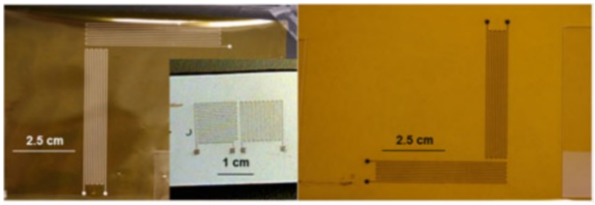

Fig. 13.9 Optical images of longitudinal and transverse strain gages: (*left*) printed silver on Kapton film and on a composite fiberglass-epoxy wind turbine blade section, and (*right*) printed constantan (Cu 55 %, Ni 45 %) on Kapton

Table 13.2 Summary of 4-element and 2-element printed strain gage values

Sample ID	Bridge elements	Design value	Measured resistance values
6A	1–4	1,000 Ω	1,000.4 Ω, 1,001.2 Ω, 1,001.5 Ω, 1,000.3 Ω
6B	1–4	1,000 Ω	1,001.4 Ω, 1,001.7 Ω, 1,002.4 Ω, 1,001.8 Ω
6C	1–2	120 Ω	122.4 Ω, 115.7 Ω

case, a 3.5 V excitation was used, with a bridge gain of 100. The resulting loading curves for the first cycle and second through fourth cycles are shown in Figs. 13.10 and 13.11.

For these samples, both high precision resistor values and highly linear strain sensing was demonstrated. Hysteresis, indicated by a small jump in voltage/resistance at a strain level of 0.0004 in Fig. 13.10, is observed in the first extension cycle, during which it is possible the printed silver undergoes some loss of network connectivity. Further fatigue testing would be of interest to evaluate long-term reliability of these printed strain gages.

An important consideration for such strain gages is the ability to both measure strain on an actual, in-operation 13–60 m rotating turbine blade, and to transmit this data remotely to an acquisition node. In addition, the ability to measure dense arrays of strain gages with a single transmitter would be of interest to accurately map blade "shape" to generate the real-time three dimensional deformation and determine true, real-time blade deflection.

A method to achieve these objectives was identified and briefly evaluated under this program. Recently, both wireless strain gage monitors, and energy-harvesting, self-powered wireless strain gage monitors have been developed by several companies for remote monitoring of industrial and structural products. Commercial off the shelf (COTS) systems exist for high-rate, real-time monitoring and data streaming of 120 Ω, 350 Ω, and 1 kΩ gauges, including integrated systems available from Microstrain, EnOcean, and Perpetuum. One of these systems, a Microstrain SG-Link, which can monitor up to eight strain gages simultaneously, and transmit data at a 4 kHz rate via 2.4 GHz to a universal serial bus (USB) receiver plugged into any personal computer, laptop, or other digital computing device. A methodology to retrieve this data from a printed network of strain gages down the length of a wind turbine blade is shown in Fig. 13.12.

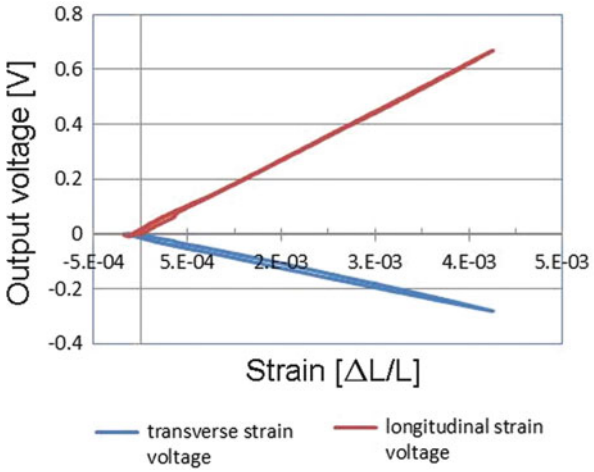

Fig. 13.10 First cycle of transverse and longitudinal strain measured by printed silver 1,000 Ω strain gage Wheatstone bridge

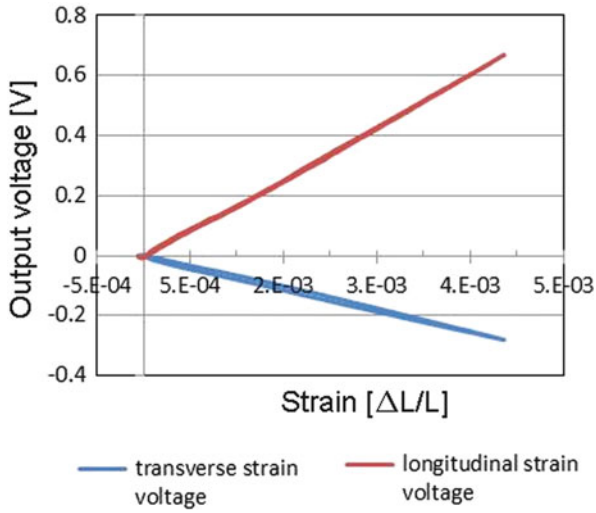

Fig. 13.11 Second, third and fourth cycles of transverse and longitudinal strain measured by printed silver 1,000 Ω strain gage Wheatstone bridge

For these SG-Link devices, an internal 600 mA-h AA Li cell is used, which provides 2–5 years of battery life for a 2.4 GHz transmission range of 70–500 m, at a 4 kHz transmission rate. For eight gages, transmission rate would be reduced to 500 Hz, but battery life would be decreased roughly twofold, requiring battery replacement consistent with normal quarterly to annual wind turbine maintenance schedules.

An attractive alternative option may be the use of new, energy-harvesting transmission nodes, such as the Microstrain EH-Link™, which may accept energy generated by vibrational (piezoelectric or inductive) generation on each rotation of the turbine, or by photovoltaic panels. As a thought experiment, a design using an integrated, 1 square foot, amorphous silicon photovoltaic panel, such as that

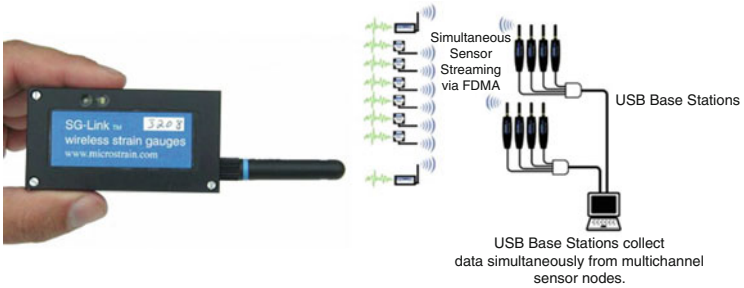

Fig. 13.12 *Left*, image of Microstrain SG-Link wireless strain gage transmitter, and, *Right*, methodology of monitoring up to 64 strain gages simultaneously: 8 gages per monitoring SG-Link uplink, and 8 receiving antennas per computer on two USB connections

manufactured by Powerfilm, was developed. An EH-Link^{TM} 8 strain gage system (Fig. 13.13) requires a 5 V power supply, with 25 mA for data streaming and 3 mA for each of eight channels, which equates to 5 V [25 mA + 8(3 mA)] = 245 mW or 0.6 W-h/day. Powerfilm produces a 5 V output, 10 W, 60 × 12.5 cm module which would produce this level of power in only 33 min of sunlight per day, appropriate even for cloudy climates. Alternatively, in full sunlight, sufficient power may be available from the same system to power 20 nodes, with eight nodes each, or a 160 strain gage array. Energy harvesting appears feasible at a cost of only around $5–100 per 8-sensor node, plus the $100–500 cost of each node.

It appears printed strain gages may hit the required 120 Ω or 1,000 Ω values needed for this implementation, and the that the transmission distance (70–500 m) is compatible with transmission from any point on a 9–60 m turbine blade to a USB receiver in the nacelle of a wind turbine. This capability for wireless, dense strain gage, high fidelity (0.5–4 kHz sampling) remote monitoring of wind turbine blades is hoped to enable calculation of real-time blade shape, deflection, vibration states, and damage levels, which would be additional inputs into smart turbine blade diagnostics and performance optimization systems. With further development, temperature and air speed wireless monitoring could also be developed as printed sensors.

13.5 Summary of Research Progress

Printing of solution precursors via inkjet, gravure printing, offset printing, microcontact printing and nanotransfer printing enables integration of many functional oxide and metal components without need for lithography or screen printing. Printing of solution precursors has recently been successfully applied to RFID tags/antennas, solar cells, thermocouples, conductive interconnects, superconductors, displays, transistors, and waveguides. Development of low vapor pressure precursors with low surface tension enables reliable printing via aerosol and contact

Fig. 13.13 *Left*, an energy harvesting-compatible, 8-strain gage wireless transmission node, and at *right*, a flexible, conformal 5 V output amorphous silicon photovoltaic system with sufficient power to power a single node from 40 min of sunlight per day

printing methods. Modifying precursor chemistry to enable low-temperature decomposition of nanoparticle surfactants and solution precursors enables integration of metallic components with low T_g polymeric substrates. While the traditional thermal route for metal conversion has been discussed, alternative conversation routes are emerging including microwave sintering, electrical conversion, and laser-sintering. These low-temperature, low thermal budget routes enable advanced integration capabilities on semiconductor, polymer, and composite materials.

By combining solution chemistry, metal nanoparticle solutions, and robotic direct printing technologies, the capability to directly print functional metal and metal oxide thin films to produce thermocouples, strain gages, and crack sensors on polymers, semiconductors, oxides, and composite materials has been demonstrated. This capability may have widespread impact on printable electronics for displays, flexible electronics, integrated microelectronics, and sensors. As an example of potential novel applications, printed nanomaterial ink traces have been highly engineered to enable achievement of precision resistors with less than 1 % variation from specification, which enabled printing of strain gage Wheatstone bridges directly on wind turbine blade composite sections. The printed gages were analyzed by traditional load-frame testing at 5,000 pound loads, and, after a first strain cycle, demonstrated reliable, linear sensing of longitudinal and transverse strain levels at all strain levels up the maximum, 0.44 % strain level tested, consistent with maximum strain tolerance required in real wind turbine blades.

For these conductive samples, both high precision resistor values and highly linear strain sensing were demonstrated. Additional work is necessary to continue development of this method, including measurements over thousands of cycles, detailed characterization of expected failure modes including printed gage delamination, and development of suitable encapsulation to avoid surface damage from debris/wind storms which real turbine blades must withstand. In addition, it is of interest to further explore the use of printed gages as binary (short circuit to open circuit) or analog (subsequent resistors which are opened as cracks extend) printed crack sensors. Conductor applications including continuous nondestructive evaluation and monitoring of wind turbine blades, industrial/utility equipment and piping may be enabled by this technology.

The potential power of this method is widespread, large area printing of functional materials on nontraditional substrates, including polymers, metals, papers, fabrics and composites. Careful use of chemical precursors, high surface area nanoparticle inks, reactive inks, and low temperature or non-thermal processing of inks (IR, UV, and microwave heating) enables processing of high performance materials on low temperature substrate materials. Extension of these methods to transparent conductors and dielectrics is currently underway by several groups, with implications for low cost electronics using lithography-free electronic materials patterning for sensor, display and logic applications.

References

1. Dominguez O, Champion Y, Bigot S (1999) Surface effects on the sintering behavior of nanometric metallic particles. Rev Mex Fis 45:74–77
2. Perelaer J, de Laat AWM, Hendriks CE, Schubert US (2008) Inkjet-printed silver tracks: low temperature curing and thermal stability investigation. J Mater Chem 18:3209–3215
3. Wakuda D, Kim KS, Suganuma K (2010) Ag nanoparticle paste synthesis for room temperature bonding. IEEE Trans Compon Packag Technol 33(2):437–442
4. Raveendran P, Fu J, Wallen SL (2003) Completely 'green' synthesis and stabilization of metal nanoparticles. J Am Chem Soc 125:13940–13941
5. Bell N, Lu P (2013) Green chemical synthesis of silver nanoparticles via maltodextrin reduction (manuscript in preparation)
6. Teng KF, Vest RW (1988) Metallization of solar-cells with ink jet printing and silver metallo-organic inks. IEEE Trans Compon Hybrids Manuf Technol 11:291–297
7. Dearden AL, Smith PJ, Shin DY (2005) A low curing temperature silver ink for use in ink-jet printing and subsequent production of conductive tracks. Macromol Rapid Commun 26 (4):315–318
8. Derby B (2011) Inkjet printing ceramics: from drops to solid. J Eur Ceram Soc 31:2543–2550
9. Vandaele K, Mosiadz M, Hopkins SC, Patel A, Van Driessche I, Glowacki BA (2012) The influence of heat treatment parameters on pyrolysed TFA-derived YBCO films deposited by inkjet printing. Mater Res Bull 47:2032–2039
10. Mosiadz M, Tomov RI, Hopkins SC, Martin G, Hardeman D, Holzapfel B, Glowacki BA (2010) Inkjet printing of $Ce_{0.8}Gd_{0.2}O_2$ thin films on Ni-5%W flexible substrates. J Sol-Gel Sci Technol 54:154–164
11. Avis C, Jang J (2011) High-performance solution processed oxide TFT with aluminum oxide gate dielectric fabricated by a sol-gel method. J Mater Chem 21:10649–10652
12. Hoffmann RC, Dilfer S, Schneider JJ (2011) Transparent indium tin oxide as inkjet-printed thin film electrodes for organic field-effect transistors. Phys Status Solidi A 208:2920–2925
13. Han SY, Lee DH, Herman GS, Chang CH (2009) Inkjet-printed high mobility transparent-oxide semiconductors. J Displ Technol 5:520–524
14. Chang NA, Richardson J, Clem PG, Hsu JWP (2005) Additive patterning of conductors and superconductors by solution stamping nanolithography. Small 2:75–79
15. Rumsey MA, Paquette JA (2008) Structural health monitoring of wind turbine blades. Proc SPIE 6933:69330E
16. White JR, Adams DE, Rumsey MA (2009) Operational load estimation of a smart wind turbine rotor blade. Proc SPIE 7295:72952D
17. Moor GD, Beukes HJ (2004) Maximum power point trackers for wind turbines. 2004 IEEE 35th annual power electronics specialists conference (IEEE Catalog. No. 04CH37551), vol 3. pp 2044–2049